Research Article Vol. 35, No. 2 / February 2018 / Journal of the Optical Society of America B 391

Journal of the Optical Society of America B

OPTICAL PHYSICS

Anomalous scaling laws of hyperbolic metamaterials in a tubular geometry

Shiwei Tang,[1,5] Yangfu Fang,[2] Lei Zhou,[3] Zhaowei Liu,[4] and Yongfeng Mei[2,6]

[1]Department of Physics, Faculty of Science, Ningbo University, Ningbo 315211, China
[2]Department of Materials Science, Fudan University, Shanghai 200433, China
[3]State Key Laboratory of Surface Physics and Key Laboratory of Micro and Nano Photonic Structures (Ministry of Education), Fudan University, Shanghai 200433, China
[4]Department of Electrical and Computer Engineering, University of California, San Diego, 9500 Gilman Drive, La Jolla, California 92093-0407, USA
[5]e-mail: tangshiwei@nbu.edu.cn
[6]e-mail: yfm@fudan.edu.cn

Received 16 October 2017; accepted 30 December 2017; posted 3 January 2018 (Doc. ID 309225); published 29 January 2018

Hyperbolic metamaterials (HMM) can be used to control light propagations in emerging meta-devices and thus lead to various functionalities (e.g., hyperlens and cloaking devices). Here we propose a kind of exotic tubular cavity by using multilayered HMM, which contrasts with traditional materials with elliptical dispersion. In such tubular microcavities, the calculations reveal that they have anomalous scaling laws, such as that the higher-order resonance mode oscillates at a longer wavelength and the resonant wavelengths hold their positions with changing the tube wall thickness and diameter. These findings can help the understanding of tubular metamaterials and could inspire interesting optical experiments and metadevices.

OCIS codes: (160.3918) Metamaterials; (160.1190) Anisotropic optical materials; (140.3945) Microcavities.

https://doi.org/10.1364/JOSAB.35.000391

1. INTRODUCTION

Nanotechnology has led to exciting developments in fundamental research including the ability to create artificial structures called metamaterials [1], which can manipulate material properties in a fantastical way. Various interesting phenomena have been discovered, such as negative index of refraction [2], invisibility cloaks [3], superlenses [4], metasurfaces [5], etc. It has been noted that a multilayered superlattice with layers of the thickness of the deep subwavelength scale can lead to anisotropic metamaterials that cannot be found in nature [6]. The most important kind of multilayered metamaterial is the one with hyperbolic dispersion [7,8], which is called a hyperbolic metamaterial (HMM). The HMMs can roll up into a hollow cylinder and form a tubular microcavity [9,10], which can serve as hyperlens [11,12], imaging objects beyond the traditional diffraction limit. Such HMMs' tubular cavity can be produced by self-roll-up processes [13–18]. The anomalous resonance properties in the rectangular and disklike nanocavities made by HMMs have been studied recently [7,19]. However, there are few reports on the resonance and propagation properties in HMM structures with tubular geometries, which could be applied to design novel opto-electrical devices for plasmonic lasers [20], biological detection [21], metamaterial fiber [22], and micro/nanomotors [23].

Two-dimensional multilayered metamaterials can be approximated and investigated by using an effective media theory [6,24,25], which can also be applied to three-dimensional structures such as superlattice cylinders [26,27]. Careful design enables deliberate tuning of the effective permittivities in such tubular HMM cavities. In this paper, we implement the Mie scattering theory and effective media theory to explore the optical resonances in the multilayered tubular cavities with anisotropic metamaterials, including HMMs. Abnormal whispering gallery mode (WGM) was observed, such as that the cavity resonance is independent on the tube size and a higher-order resonance mode oscillates at a longer wavelength. Our exploration could lead to deep understanding and novel devices by using tubular metamaterials.

2. THEORETICAL ANALYSIS AND NUMERICAL RESULTS

The multilayered tubular microcavity is sketched in Fig. 1(a). A single bilayer unit is composed by a layer A and a layer B, where ε_A, ε_B are the corresponding permittivities and d_A, d_B are the thicknesses. The materials in layers A and B can be metal, dielectric, or semiconductor. We assume permeability $\mu = 1$ and only consider the permittivity ε variance of the

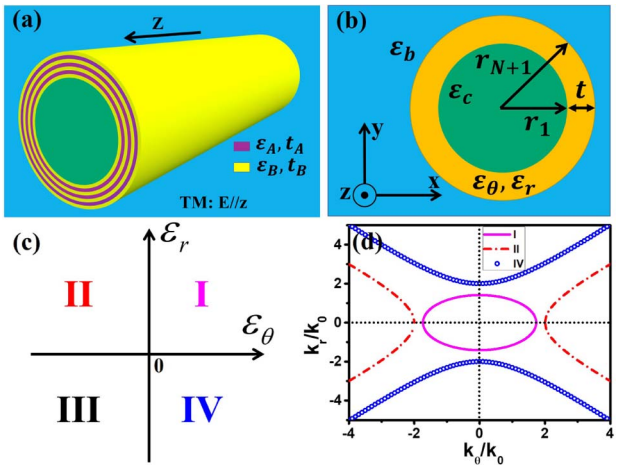

Fig. 1. (a) Schematic cross section of a multilayered hollow cylinder structure; (b) the cylinder structure can be treated as an anisotropic metamaterial; (c) the different regions of effective permittivities, which can be achieved with the designed anisotropic metamaterials; (d) the schematic dispersion relation curves are plotted for Region I (magenta line, $\varepsilon_\theta = 3$, $\varepsilon_r = 2$), Region II (red dashed–dotted line, $\varepsilon_\theta = -3$, $\varepsilon_r = 4$), and Region IV (blue circle symbols, $\varepsilon_\theta = 4$, $\varepsilon_r = -3$).

designed metamaterials. We take the permittivities of the core and background outside of the hollow cylinder as ε_c and ε_b, respectively [see Fig. 1(b)]. When the individual bilayer thickness is much smaller than the wavelength, an effective permittivity can be approximated using an effective media theory. The effective media theory allows us to calculate the radial and tangential permittivity of the multilayered hollow cylinder structure in the following way:

$$\varepsilon_\theta = \varepsilon_z = \frac{d_A\varepsilon_A + d_B\varepsilon_B}{d_A + d_B} \quad \varepsilon_r = \frac{\varepsilon_A\varepsilon_B(d_A + d_B)}{d_A\varepsilon_B + d_B\varepsilon_A}. \tag{1}$$

We may consider the nonlocal adjustment to such an effective media model if the multilayer hollow cylinder has a small radius [28]. But we will demonstrate that the effective media theory of Eq. (1) is accurate enough for the very thin layers in our designs in the following discussion.

As a result, the multilayer hollow cylinder structure can be treated as an anisotropic metamaterial [Fig. 1(b)] whose permittivities ε_θ and ε_r are determined by the effective media theory.

We consider transverse magnetic (TM) waves that are propagating in the $r-\theta$ plane with the magnetic field along the z direction, where the electric field vector can be divided into two components (along and transverse to the optical axis of the tube). As a result, both ε_θ and ε_r play a role in the dielectric response. Using the effective media theory, the dispersion relation for TM polarization is given by

$$\frac{k_\theta^2}{\varepsilon_r} + \frac{k_r^2}{\varepsilon_\theta} = \frac{\omega^2}{c^2}. \tag{2}$$

Figure 1(c) shows that several kinds of materials can be divided into four regions according to the signs for ε_θ and ε_r. For the conventional material with $\varepsilon_r > 0$ and $\varepsilon_\theta > 0$ (Region I), the dispersion relationship is elliptic. However, when $\varepsilon_r > 0$ and $\varepsilon_\theta < 0$ (Region II), it leads to a HMM with the foci in the axis of k_θ; similarly, when $\varepsilon_r < 0$ and $\varepsilon_\theta > 0$ (Region IV), it leads to a HMM with the foci in the axis of k_r. The dispersion relationships of these three regions are shown in Fig. 1(d). Region III with ε_r and ε_θ are both negative, and it arises from tubular microcavities made of metals [29].

We employ rigorous Mie scattering theory to quantitatively study the optical properties of our tubular cavities in different regions. The tubular cavity can be viewed as a multilayered structure in a cylindrical geometry with $(N-1)$ layers and the layer indexed by i. The indices of the core and background are 1 and $(N+1)$, respectively. The ith layer has an outer radius of r_i and the dielectric constant ε_i, while the tubular cavity is along the z direction for simplicity.

When the TM waves impact the cavity, the magnetic field in the ith layer can be expressed as

$$H_{i,z} = \sum_{m=0}^{\infty}(a_{i,m}J_m(k_i r) + b_{i,m}H_m^{(1)}(k_i r))e^{im\theta}, \tag{3}$$

where $k_i = \sqrt{\varepsilon_i}k_0$. The origin of the cylindrical coordinates (r,θ) is at the center of tubular cavity, and the Bessel function J_m and Hankel function $H_m^{(1)}$ of the first kind stand for the incident and scattering waves, respectively. The resonances occur in the tubular cavity when

$$k_\theta = \frac{2\pi m}{L}, \tag{4}$$

where $L = \pi(r_1 + r_N) = \pi(2R + t)$ and where m is the angular momentum mode number, and k_θ is the tangential component of the wave vector.

Using continuities of H_z and $\frac{1}{\varepsilon}\frac{\partial}{\partial r}H_z$, we have

$$\frac{J_m'(k_{i+1}r_i) + D_{i+1,m}H_m^{(1)\prime}(k_{i+1}r_i)}{J_m(k_{i+1}r_i) + D_{i+1,m}H_m^{(1)}(k_{i+1}r_i)} = \frac{\alpha_i}{\alpha_{i+1}}\frac{J_m'(k_i r_i) + D_{i,m}H_m^{(1)\prime}(k_i r_i)}{J_m(k_i r_i) + D_{i,m}H_m^{(1)}(k_i r_i)}, \tag{5}$$

where $D_{i,m} = b_{i,m}/a_{i,m}$, $\alpha_i = k_i/\varepsilon_i$. Using $D_{1,m} = 0$, we can obtain the scattering coefficient $D_{N+1,m}$ of the tubular cavity. The total absorption cross section of the tubular cavity is obtained by the following relationship [30]:

$$C_a = \frac{\lambda}{2\pi}\sum_{m=0}^{\infty}(1 - |2D_{N+1,m} + 1|^2). \tag{6}$$

In the following, we focus on the material combinations with hyperbolic dispersion relations (Regions II and IV). Such HMMs [31] enable photonic structures with unusual features, including adiabatic wavelength compression and highly confined guided modes with very large cutoffs [32,33], which are due to the unbounded values of wave vector k at a finite frequency, and thus allowed by the hyperbolic dispersion relation.

We take Region II ($\varepsilon_r > 0$, $\varepsilon_\theta < 0$) as an example. We take the doped semiconductor works at the terahertz (THz) region as layer A, whose dielectric constant can be described by the Drude model $\varepsilon_r(\omega) = \varepsilon_\infty - \omega_{\mathrm{pl}}^2/(\omega^2 - i\omega\omega_{\mathrm{col}})$ with plasmon frequency $\omega_{\mathrm{pl}} = 1.6\times10^{14}$ rad/s^{-1}, damping parameter $\omega_{\mathrm{col}} = 2.18\times10^{10}$ rad/s^{-1} and $\varepsilon_\infty = 1$ [34]. The dielectric

constant for layer B in the bilayer is $\varepsilon_B = 1.96$, while the thicknesses of the single bilayer are $d_A = 100$ nm, $d_B = 800$ nm.

Here, we take the core and background materials of the hollow cylinder structure as air ($\varepsilon_b = \varepsilon_c = 1$). The radius of the core and tube wall thickness of the hollow cylinder structure are set as $r_1 = 155$ μm, $t = 40$ μm, which can be abbreviated as (155, 40) μm. For this case, the absorption cross sections of the angular momentum modes $m = 16$ in the THz region are calculated and plotted in Fig. 2(a).

In order to demonstrate that the effective media theory is accurate enough, we have to perform simulations for cavities formed by homogeneous materials with permittivity provided by effective medium theory and directly compare with rigorous results obtained using Mie theory.

For the TM mode, H_z should satisfy the following equation:

$$\frac{1}{\mu_z}\frac{1}{r}\frac{\partial}{\partial r}\left(\frac{r}{\varepsilon_\theta}\frac{\partial H_z}{\partial r}\right) + \frac{1}{\mu_z}\frac{1}{r^2}\frac{\partial}{\partial \theta}\left(\frac{1}{\varepsilon_r}\frac{\partial H_z}{\partial \theta}\right) + k_0^2 H_z = 0. \quad (7)$$

Using the separation variable method and substitution: $H_z = y(r)e^{-im\theta}$, $x = k_0\sqrt{\varepsilon_\theta \mu_z} r$, and $\mu_z = 1$, we can get

$$x^2 y'' + xy' + \left(x^2 - m^2\frac{\varepsilon_\theta}{\varepsilon_r}\right)y = 0, \quad (8)$$

which is a complex-order Bessel function when $\varepsilon_r > 0$, $\varepsilon_\theta < 0$. We can calculate the function based on two kinds of series expansions and numerical integration [35]. Then the absorption cross sections of the homogeneous materials with permittivity provided by effective medium theory are calculated and plotted in Fig. 2(a), which are in excellent agreement with results calculated by Mie theory from the multilayer structure. Such agreement supports that all the discussions can be based on the effective media theory.

From Fig. 2(a) we also can find that for the angular momentum mode $m = 16$, there are two peaks within a certain wavelength range. The magnetic field distributions of these two peaks are presented in Figs. 2(b) and 2(c), which correspond to two radial resonance modes. The mode number of the radial resonance mode is set as n. If the magnetic field can be bound in the tube wall, the wave vector k_r can be written as

$$k_r = \frac{\pi n}{t}. \quad (9)$$

Using resonance mode numbers m and n, we can figure out all peaks in Fig. 2(a). We can abbreviate the modes $m = 16$, $n = 1$ and $m = 16$, $n = 2$ as modes {16, 1} and {16, 2}. From Figs. 2(a)–2(c) we can find that the resonance mode at wavelength of 114.6 μm is mode {16, 1} and the mode at 142 μm is the higher-order radial resonance mode {16, 2}.

Using Eq. (1), we can obtain the effective radial and tangential permittivities of such structure. The effective parameters for the working wavelength 114.6 μm are $\varepsilon_\theta = -8.7 + 0.0141i$, $\varepsilon_r = 2.21$, and for the working wavelength 142 μm are $\varepsilon_\theta = -14.36 + 0.0267i$, $\varepsilon_r = 2.2$, which can satisfy the conditions of Region II. As a result, in Region II, higher-order radial resonance mode oscillates at a longer wavelength compared to the lower-order mode, which is different from traditional materials.

In order to clarify such phenomenon, we picked a material from Region I that also has resonance mode {16, 2} and oscillates at the same wavelength of 142 μm. We take the dielectric constants of the single bilayer as $\varepsilon_A = \varepsilon_B = 14.8 + 0.01i$. The thicknesses of each layer in the bilayer structure are the same as in the Region II case. In this case, the absorption cross sections of the angular momentum modes $m = 16$ and $m = 17$ are calculated and plotted in Fig. 3(e). For each angular momentum mode, we can find multiple peaks within the certain wavelength range. The magnetic field distributions of these peaks are presented in Figs. 3(a)–3(d), which are corresponding to modes {16, 1}, {16, 2}, {17, 2}, and {17, 3}. From the absorption cross sections and magnetic field distributions, we can figure out that in Region I the higher-order angular momentum mode {17, 2} is in the shorter wavelength compared to the mode {16, 2}, and a higher-order radial resonance mode {16, 3} oscillates at the shorter wavelength compared to {16, 2}, as well.

The absorption cross sections of the angular momentum modes $m = 16$ and $m = 17$ in Region II are calculated and

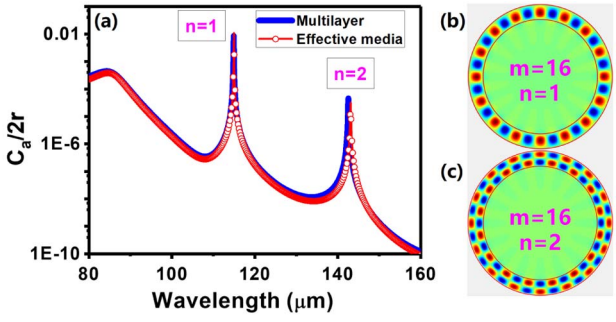

Fig. 2. (a) The absorption cross sections of mode $m = 16$ for Region II from the multilayer structure (blue line) and homogeneous materials with permittivity provided by effective medium theory (red circle). (b, c) Calculated magnetic field distributions of different modes for cavities in Region II.

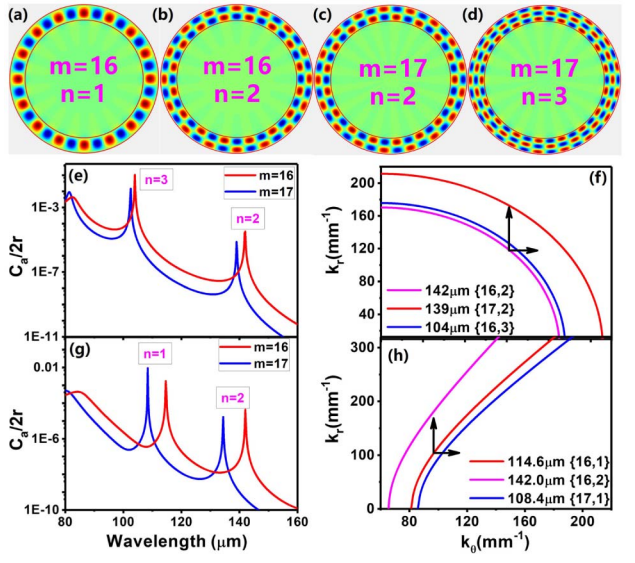

Fig. 3. (a)–(d) Calculated magnetic field distributions of different modes for cavities in Region I; the absorption cross sections for Region I (e) and Region II (g); the dispersion relationship for Region I (f) and Region II (h) at various wavelengths.

plotted in Fig. 3(g). We can find that the higher-order angular momentum mode {17, 2} is in the shorter wavelength compared to the mode {16, 2}, which is the same as Region I. However, a lower-order radial resonance mode {16, 1} oscillates at the shorter wavelength compared to mode {16, 2}, which is different from the materials in Region I.

In order to explain the phenomena above, we present the dispersion relationship Eq. (2) of Region I and II at different resonance wavelengths in Figs. 3(f) and 3(h). By using Eq. (4), we can find when the angular momentum mode order m increases; a significant increase in k_θ causes the higher-order mode to oscillate at a shorter wavelength for both Region I and II. But if we keep k_θ fixed and try to make the radial momentum mode order n increase, this drives the k_r growth due to Eq. (9). In this case, from Fig. 3(f) we can find that the resonance wavelength goes to the shorter wavelength for Region I. But as shown in Fig. 3(h), the resonance wavelength goes to the longer wavelength in Region II, which is exactly opposite to the case of the Region I. As a result, we can find the reason that the higher-order radial mode oscillates at a longer wavelength in Region II from the dispersion relationship.

Meanwhile, the dispersion relationship of Region IV has a similar feature to Region II, except that the foci is in the axis of k_r instead of k_θ. So we can figure out that the radial resonance behavior in Region IV is the same as in Region I, but the higher-order angular momentum mode oscillates at a longer wavelength in Region IV.

With the HMM in the Region II, higher-order radial resonance mode can oscillate at a longer wavelength, while the modes for the tubular cavities are independent on the tube diameters and present the same resonant peaks. Figure 4 shows that the cavities resonate for the {16, 2} modes with different tube radii and wall thicknesses (r_1, t). In Fig. 4(a), a larger cavity (bigger diameters) has a longer resonant wavelength for a given mode order for the conventional optical cavities (Region I), but the refractive index is not strongly related to the cavity size. As for the cavities with HMM (Region II), all of the {16, 2} modes for different cavities in diameter resonate at the same wavelength of 142 μm, which are shown in Fig. 4(b). From the dispersion relationship Eq. (2) and $\varepsilon_r > 0$, $\varepsilon_\theta < 0$ in Region II, it can be understood that as the cavity size shrinks, both k_θ and k_r scale up simultaneously to maintain the cavity resonant wavelength [7]. The same phenomena of different size cavities having the same resonant wavelength can also be observed in Region IV.

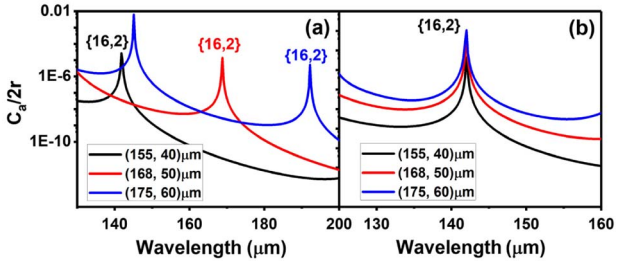

Fig. 4. Absorption cross sections for the tubular cavities in Region I (a) and Region II (b) with different diameters.

3. CONCLUSIONS

In summary, we have applied the Mie scattering method and effective media theory to explore the abnormal optical resonance properties in the tubular microcavities with anisotropic metamaterials. In contrast to traditional materials, tubular microcavities with HMM present that the cavity resonance is independent on the tube sizes and a higher-order resonance mode oscillates at a longer wavelength. These properties we discussed can guide future experiments and open up new possibilities for nanophotonic applications in optical communications [12], biosensing [36], optomechanics [37], and cavity optical nonlinearities [38].

Funding. National Natural Science Foundation of China (NSFC) (61628401, 51475093, U1632115, 11474057, 11674068, 11604167); Science and Technology Commission of Shanghai Municipality (STCSM) (14JC1400200); K. C. Wong Magna Fund in Ningbo University; Changjiang Young Scholars Programme of China.

REFERENCES

1. J. B. Pendry, "Negative refraction," Contemp. Phys. **45**, 191–202 (2004).
2. D. R. Smith, W. J. Padilla, D. C. Vier, S. C. Nemat-Nasser, and S. Schultz, "Composite medium with simultaneously negative permeability and permittivity," Phys. Rev. Lett. **84**, 4184–4187 (2000).
3. D. Schurig, J. J. Mock, B. J. Justice, S. A. Cummer, J. B. Pendry, A. F. Starr, and D. R. Smith, "Metamaterial electromagnetic cloak at microwave frequencies," Science **314**, 977–980 (2006).
4. J. B. Pendry, "Negative refraction makes a perfect lens," Phys. Rev. Lett. **85**, 3966–3969 (2000).
5. S. L. Sun, Q. He, S. Y. Xiao, Q. Xu, X. Li, and L. Zhou, "Gradient-index meta-surfaces as a bridge linking propagating waves and surface waves," Nat. Mater. **11**, 426–431 (2012).
6. A. Poddubny, I. Iorsh, P. Belov, and Y. Kivshar, "Hyperbolic metamaterials," Nat. Photonics **7**, 948–957 (2013).
7. X. Yang, J. Yao, J. Rho, X. Yin, and X. Zhang, "Experimental realization of three-dimensional indefinite cavities at the nanoscale with anomalous scaling laws," Nat. Photonics **6**, 450–454 (2012).
8. D. Lu, J. J. Kan, E. E. Fullerton, and Z. Liu, "Enhancing spontaneous emission rates of molecules using nanopatterned multilayer hyperbolic metamaterials," Nat. Nanotechnol. **9**, 48–53 (2014).
9. G. S. Huang and Y. F. Mei, "Thinning and shaping solid films into functional and integrative nanomembranes," Adv. Mater. **24**, 2517–2546 (2012).
10. Y. F. Mei, G. S. Huang, A. A. Solovev, E. B. Ureña, I. Mönch, F. Ding, T. Reindl, R. K. Y. Fu, P. K. Chu, and O. G. Schmidt, "Versatile approach for integrative and functionalized tubes by strain engineering of nanomembranes on polymers," Adv. Mater. **20**, 4085–4090 (2008).
11. Z. Liu, H. Lee, Y. Xiong, C. Sun, and X. Zhang, "Far-field optical hyperlens magnifying sub-diffraction-limited objects," Science **315**, 1686 (2007).
12. E. J. Smith, Z. Liu, Y. F. Mei, and O. G. Schmidt, "System investigation of a rolled-up metamaterial optical hyperlens structure," Appl. Phys. Lett. **95**, 083104 (2009).
13. Z. Tian, L. Zhang, Y. Fang, B. Xu, S. Tang, N. Hu, Z. An, Z. Chen, and Y. Mei, "Deterministic self-rolling of ultrathin nanocrystalline diamond nanomembranes for 3D tubular/helical architecture," Adv. Mater. **29**, 1604572 (2017).
14. J. Wang, E. Song, C. Yang, L. Zheng, and Y. Mei, "Fabrication and whispering gallery resonance of self-rolled up gallium nitride microcavities," Thin Solid Films **627**, 77–81 (2017).
15. G. Huang and Y. Mei, "Electromagnetic wave propagation in a rolled-up tubular microcavity," J. Mater. Chem. C **5**, 2758–2770 (2017).

16. X. Lin, Y. Fang, L. Zhu, J. Zhang, G. Huang, J. Wang, and Y. Mei, "Self-rolling of oxide nanomembranes and resonance coupling in tubular optical microcavity," Adv. Opt. Mater. **4**, 936–942 (2016).
17. Y. Fang, S. Li, and Y. Mei, "Modulation of high quality factors in rolled-up microcavities," Phys. Rev. A **94**, 033804 (2016).
18. Y. Fang, S. Li, S. Kiravittaya, and Y. Mei, "Exceptional points in rolled-up tubular microcavities," J. Opt. **19**, 095101 (2017).
19. C. Bacco, P. Kelly, and L. Kuznetsova, "Optical mode confinement in three-dimensional Al/SiO_2 nano-cavities with hyperbolic dispersion," Proc. SPIE **9544**, 954419 (2015).
20. V. J. Sorger and X. Zhang, "Spotlight on plasmon lasers," Science **333**, 709–710 (2011).
21. A. F. Abouraddy, M. Bayindir, G. Benoit, S. D. Hart, K. Kuriki, N. Orf, O. Shapira, F. Sorin, B. Temelkuran, and Y. Fink, "Towards multimaterial multifunctional fibres that see, hear, sense and communicate," Nat. Mater. **6**, 336–347 (2007).
22. E. J. Smith, Z. Liu, Y. Mei, and O. G. Schmidt, "Combined surface plasmon and classical waveguiding through metamaterial fiber design," Nano Lett. **10**, 1–5 (2010).
23. J. X. Li, W. Gao, R. F. Dong, A. Pei, S. Sattayasamitsathit, and J. Wang, "Nanomotor lithography," Nat. Commun. **5**, 5026 (2014).
24. V. M. Agranovich and V. E. Kravtsov, "Notes on crystal optics of superlattices," Solid State Commun. **55**, 85–90 (1985).
25. S. W. Tang, B. C. Zhu, M. Jia, Q. He, S. L. Sun, Y. F. Mei, and L. Zhou, "Effective-medium theory for one-dimensional gratings," Phys. Rev. B **91**, 174201 (2015).
26. B. Wood, J. Pendry, and D. Tsai, "Directed subwavelength imaging using a layered metal-dielectric system," Phys. Rev. B **74**, 115116 (2006).
27. A. Salandrino and N. Engheta, "Far-field subdiffraction optical microscopy using metamaterial crystals: theory and simulations," Phys. Rev. B **74**, 075103 (2006).
28. A. V. Kildishev, U. K. Chettiar, Z. Jacob, V. M. Shalaev, and E. E. Narimanov, "Materializing a binary hyperlens design," Appl. Phys. Lett. **94**, 071102 (2009).
29. S. W. Tang, Y. F. Fang, Z. W. Liu, L. Zhou, and Y. F. Mei, "Tubular optical microcavities of indefinite medium for sensitive liquid refractometers," Lab Chip **16**, 182–187 (2016).
30. H. C. Hulst, *Light Scattering by Small Particles* (Dover, 1981).
31. D. Smith and D. Schurig, "Electromagnetic wave propagation in media with indefinite permittivity and permeability tensors," Phys. Rev. Lett. **90**, 077405 (2003).
32. V. Podolskiy and E. Narimanov, "Strongly anisotropic waveguide as a nonmagnetic left-handed system," Phys. Rev. B **71**, 201101 (2005).
33. A. Govyadinov and V. Podolskiy, "Metamaterial photonic funnels for subdiffraction light compression and propagation," Phys. Rev. B **73**, 155108 (2006).
34. M. V. Exter and D. Grischkowsky, "Optical and electronic properties of doped silicon from 0.1 to 2 THz," Appl. Phys. Lett. **56**, 1694–1697 (1990).
35. M. Kodama, "Algorithm 912: a module for calculating cylindrical functions of complex order and complex argument," ACM Trans. on Math. Software **37**, 1–25 (2011).
36. F. Vollmer and S. Arnold, "Whispering-gallery-mode biosensing: label-free detection down to single molecules," Nat. Methods **5**, 591–596 (2008).
37. K. Srinivasan, H. Miao, M. T. Rakher, M. Davanço, and V. Aksyuk, "Optomechanical transduction of an integrated silicon cantilever probe using a microdisk resonator," Nano Lett. **11**, 791–797 (2011).
38. D. O'shea, C. Junge, M. Pöllinger, A. Vogler, and A. Rauschenbeutel, "All-optical switching and strong coupling using tunable whispering-gallery-mode microresonators," Appl. Phys. B **105**, 129–148 (2011).